

Advancing lithium metal electrode beyond 99.9% coulombic efficiency via super-saturated electrolyte with compressed solvation structure

Received: 16 December 2024

Accepted: 28 April 2025

Published online: 07 May 2025

 Check for updatesWujie Yang^{1,2}, Aoyuan Chen^{1,2}, Ping He^{1,2}  & Haoshen Zhou^{1,2} 

Lithium metal negative electrode is pivotal for advancing high-energy-density lithium batteries. Despite their promise, the inherent poor interfacial stability of electrolytes on lithium metal and the repeated reconstruction of the solid electrolyte interphase lead to continuous consumption of active Li and electrolyte, causing rapid failure of Li metal batteries under practical conditions. Here, we propose compressing the spacing between Li ions and anions to recruit more anions around Li ions, forming tighter solvation clusters, and then achieving the super-saturated electrolyte with a 16 M Li salt concentration in the solvent phase. This compressed solvation structure electrolyte demonstrates enhanced stability towards Li metal negative electrode, attaining more than 99.9% coulombic efficiency in Li||Cu cells and enabling long cycling life in lean-Li Li metal full cells. Designed with a positive electrode material proportion of 68%, our Li metal pouch cell achieves a specific energy of 510.3 Wh kg⁻¹ (based on the total mass of the cell) and maintains stable cycling over 100 cycles.

As the premier candidate for lithium (Li) batteries, Li metal negative electrode (LMN) has long been regarded as the “ultimate negative electrode material”, an indispensable piece of the puzzle for achieving high-energy-density chemical power sources exceeding 500 Wh kg⁻¹. Yet, the path to the practical application of Li metal batteries (LMB) has been riddled with immense challenges. The high reactivity due to the extremely low redox potential (−3.04 V vs. the standard hydrogen electrode) results in unavoidable side reactions with the electrolytes, which severely compromise the reversibility of Li plating and stripping, and expedite the depletion of the electrolyte^{2,3}. In practical scenarios with lean electrolyte and scarce Li inventory, this further hastens the degradation of LMB^{4,5}. The inherent reduction stability of the electrolyte towards LMN, as well as the shielding effectiveness and durability of the solid electrolyte interphase (SEI) derived from the electrolyte decomposition, play a crucial role in pursuing optimal reversible LMN^{6–8}.

A multitude of promising electrolyte engineering approaches have been developed to tackle the reversibility challenges of LMN by modulating the SEI chemistry and Li deposition morphology. These strategies include high concentration electrolytes^{9,10}, localized high concentration electrolytes (LHCE)^{11,12}, fluorinated electrolytes^{13–16}, weakly solvating electrolytes^{17–19}, additive engineering^{3,20,21}, and liquified gas electrolytes^{22–24}, etc. The most central thesis is to introduce more anions into the first solvation shell of Li ions, thereby minimizing the reductive decomposition of the solvents and fostering the formation of an SEI rich in inorganics derived from anions, which ensures high ionic conductivity and electronic insulation^{25,26}. As an exemplar of success, a considerable number of reports have shown LHCEs achieving coulombic efficiency (CE) exceeding 99.5%^{11,12,27–32}. However, the prevalent LHCEs predominantly employ diluents such as fluorinated ether^{27,28,33}, fluoroalkane²⁹, or fluorobenzene^{30,34,35}, which may

¹Center of Energy Storage Materials & Technology, College of Engineering and Applied Sciences, Jiangsu Key Laboratory of Artificial Functional Materials, Nanjing University, Nanjing 210093, China. ²National Laboratory of Solid-State Microstructures and Collaborative Innovation Center of Advanced Microstructures, Nanjing University, Nanjing 210093, China. ✉ e-mail: pinghe@nju.edu.cn; hszhou@nju.edu.cn

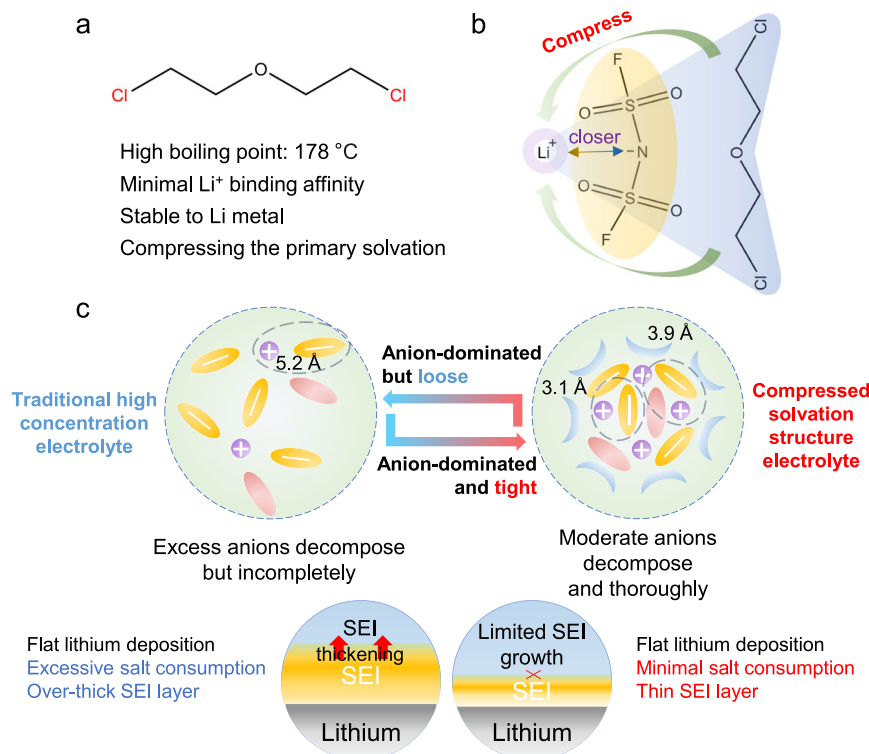


Fig. 1 | Conceptual framework and LMN stabilization rationale of the compressed solvation structure electrolyte. a Molecular features of CIDEE. **b** CIDEE closely adheres to the outer of the primary solvation shell of Li^+ , compressing the interval between Li^+ and FSI^- anions. **c** Compared to traditional concentrated electrolytes with abundant anions but a loosely packed structure, the compressed

solvation structure electrolyte features more compact, small solvation clusters. This compact arrangement accelerates the breakdown kinetics of FSI^- anion to form a robust SEI, minimizing the depletion of Li salts and the growth of the SEI, thus enabling highly reversible LMN.

participate in the SEI formation process, causing additional charge loss owing to the highest electronegativity of F. On the other hand, these F-rich diluents can diminish the solvent's ability to dissolve Li salts through dipole-dipole interactions (such as pseudo-H bonds between H and F)^{36,37}, which consequently limits the number of anions in the vicinity of Li ions somewhat. These may account for the dilemma in achieving a higher level of CE. Beyond LHCE, Cui's and Meng's groups have reported 99.9% Li CE with single-salt-single-solvent fluorinated ether electrolyte¹³ and liquified gas electrolyte²⁴, respectively. However, these two electrolyte options still encounter issues of high production costs and sophisticated operational settings. Thus far, simultaneously maximizing the effectiveness of anion-derived SEI, minimizing solvent decomposition, and enhancing the intrinsic anti-reductive property of the electrolyte to achieve an ultra-stable LMN still remains to be further explored.

Here, we report a compressed solvation structure electrolyte designed to maximize the population of anions surrounding Li ions. By squeezing the distance between Li ions and FSI^- anions, more anions can penetrate the solvation shell of Li ions, forming more compact solvation clusters, thereby increasing the solubility of Li salt in the solvent phase (Fig. 1). This compressed solvation structure not only has excellent inherent anti-reductive property but also facilitates rapid and thorough passivation of the LMN, resulting in efficient Li plating and stripping. With the unique small solvation clusters teeming with anions, such electrolyte achieves an impressive Li CE exceeding 99.9% in Li||copper (Cu) coin cell. Subsequently, in full coin cells with ultra-thin Li negative electrode (20 μm) and high-loading $\text{LiNi}_{0.83}\text{Co}_{0.12}\text{Mn}_{0.5}\text{O}_2$ (NCM811) positive electrode (2.5 mAh cm^{-2} or 3.8 mAh cm^{-2}), the electrolyte has demonstrated stable operation over 600 and 350 cycles without abrupt “rollover failure” at N/P ratios of 1.6 and 1.05, respectively, standing among the

state-of-the-art lean-Li LMB. Furthermore, by integrating lean electrolyte (1.1 g Ah^{-1}), high positive electrode loading (30 mg cm^{-2}), we have realized stable operation of Li metal pouch cell with an initial specific energy above 500 Wh kg^{-1} over 100 cycles.

Results and Discussion

Electrolyte design and solvation structure analysis

To establish a solvation framework densely packed with anions, we propose a solvation-compressed electrolyte consisting of 2 M Li bis(fluorosulfonyl)imide (LiFSI) dissolved in a mixture of dimethoxyethane (DME) and 2,2-dichlorodiethylether (CIDEE) with a volume ratio of 1:7 (denoted as Cl 7 electrolyte). The solubility of the Li salt in various solvents is initially examined (Supplementary Fig. 1). It shows that CIDEE alone has a solubility for LiFSI of less than 0.05 mol/L, which can be considered a non-solvating diluent. Additionally, when DME is mixed with 16 mol/L LiFSI, there are clearly many undissolved precipitates in the electrolyte, indicating that DME alone cannot fully dissociate such a large amount of Li salts. Yet, when DME is combined with CIDEE at a 1:7 volume ratio, 2 M LiFSI can dissolve entirely and shows a smooth flow. This signifies the attainment of a record-breaking 16 mol L^{-1} concentration of Li salts within the localized solvation phase (here, within the DME phase). Given such a high concentration of FSI^- around Li^+ , inorganic-rich robust SEI derived by decomposition of anion can be anticipated. In addition, CIDEE features a boiling point of up to 178 $^{\circ}\text{C}$ ³⁸, exceeding that of the majority of ether solvents reported, revealing its considerable potential for practical exploitation.

Since the composition of electrode/electrolyte interphases as well as the dynamic behavior of Li ion at the interface are intimately linked to the solvation structure, we undertook an in-depth analysis of the solvation structures of the electrolytes. Molecular dynamics (MD)

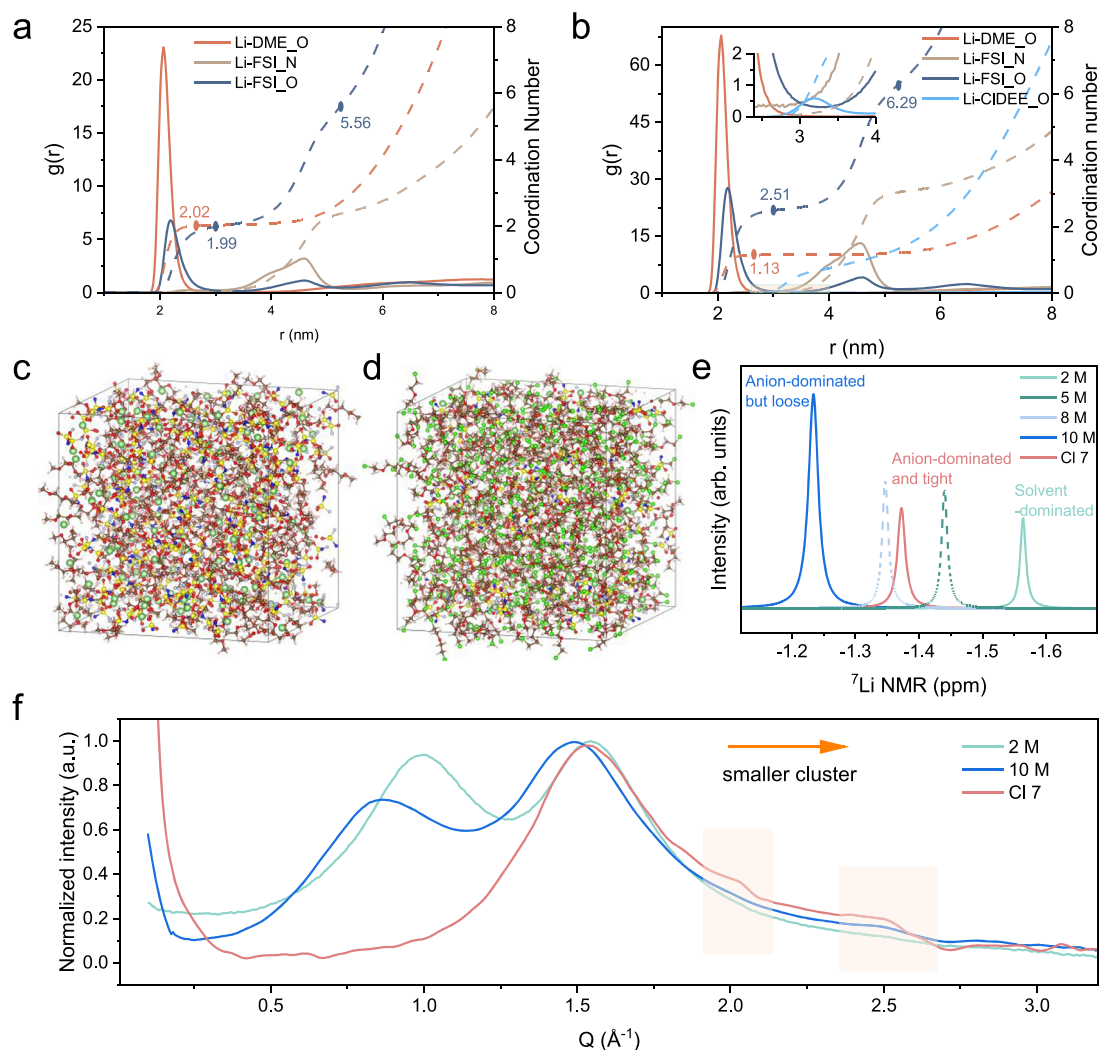


Fig. 2 | Investigation of solvation structures. Radical distribution functions ($g(r)$, solid lines) and coordination number ($n(r)$, dashed lines) in (a) 10 M electrolyte and (b) Cl 7 electrolyte. Snapshots of the MD simulation boxes of (c) 10 M and (d) Cl 7

electrolytes. **e** ^7Li NMR spectra of different electrolytes. **f** WAXS reveals the presence of a shorter interatomic correlation distance within the Cl 7 electrolyte, forming more compact solvation clusters.

simulations were carried out to inquire into the distribution scenario of anions and solvents around Li ions at the microscopic scale (Fig. 2a–d, Supplementary Fig. 2 and Supplementary Data 1). In conventional high-concentration electrolyte that is nearly saturated at room temperature (10 M LiFSI in DME, donated as 10 M electrolyte), the coordination numbers of O_{DME} at $\sim 2.06 \text{ \AA}$ and O_{FSI} at $\sim 2.19 \text{ \AA}$ are 2.02 and 1.99 respectively, reflecting a significant concentration of anions occupies the primary solvation shell of Li^+ . In the Cl 7 electrolyte, the coordination of FSI^- has become markedly stronger, with the coordination number of O_{FSI} rising to 2.51, significantly higher than 1.13 observed for O_{DME} . Moreover, the oxygen atoms from CIDEE are closely aligned beyond the primary solvation shell of Li^+ at around 3 \AA , resembling a compressed outer layer that encapsulates the primary solvation shell of Li^+ . Results from the statistical evaluation of various solvation clusters also reveal that the Cl 7 electrolyte contains a markedly greater proportion of FSI^- -dominated solvation clusters (Supplementary Fig. 3). Additionally, the presence of a significant amount of CIDEE enhances the wettability of the electrolyte with tight ion aggregation and ensures acceptable Li^+ transport properties (Supplementary Figs. 4, 5, Supplementary Note 1).

The results of the simulation calculations are further confirmed by experimental characterization. From the results of ^7Li nuclear magnetic resonance (NMR) spectra (Fig. 2e), as the concentration of LiFSI

in DME rises from 2 M to 10 M, the ^7Li peak experiences a progressive downward shift. This is attributed to the fact that FSI^- anions, which have a weaker electron cloud density compared to DME, are progressively occupying the solvation shell of Li^+ and the solvation structure evolves from solvent-dominated to anion-dominated gradually^{39,40}. However, the electron cloud density surrounding Li^+ in the Cl 7 electrolyte is noticeably higher compared to typical high-concentration electrolytes. We attribute this anomalous phenomenon to the reduced distance between Li^+ and FSI^- anions within the compressed solvation structure of the Cl 7 electrolyte, leading to the formation of smaller solvation clusters and a denser electron cloud around the Li^+ . Wide-angle X-ray scattering (WAXS) was further employed to probe the information for solvation clusters. In Fig. 2f, the WAXS results show that in traditional single-phase DME-based electrolytes, there are two typical solvation clusters corresponding to the scattering vector (Q) values around 0.9 and 1.5 \AA^{-1} (Corresponding to r values of 8.6 \AA and 5.2 \AA respectively, referring to the Ehrenfest equation $Q \cdot r = 2.46\pi$, where r is the characteristic interatomic correlation distance)^{41,42}. With the Li salt concentration increasing from 2 M to 10 M, the peaks shift towards lower Q values in totality, corresponding to the increased characteristic interatomic correlation distance. This indicates that the solvation clusters in the electrolyte have enlarged due to the incorporation of larger-sized FSI^- anions into the Li^+ solvation sheath. In

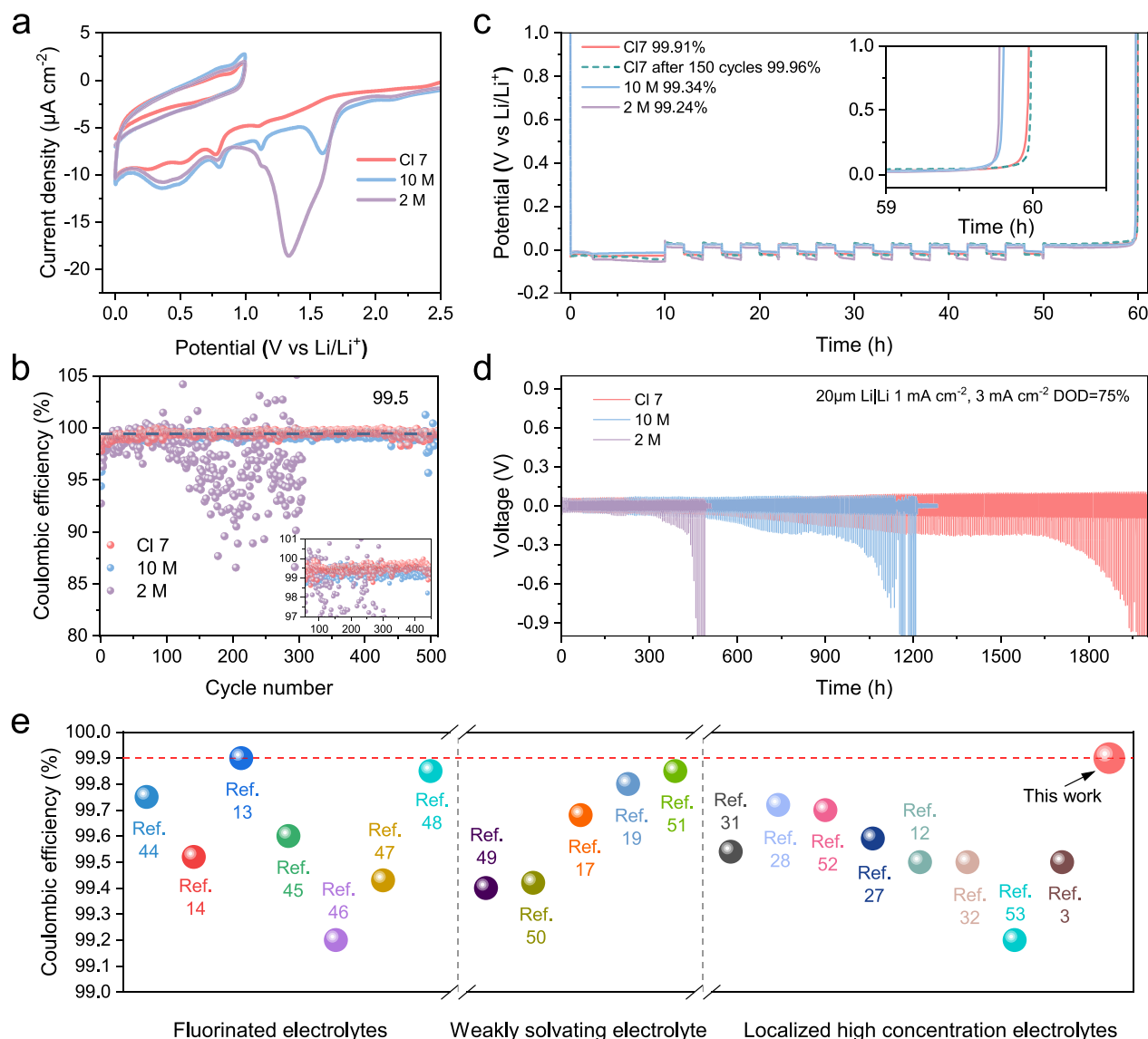


Fig. 3 | Li metal stability and reversibility of Li plating/stripping. **a** Cyclic voltammetry of the electrolytes in Li||Cu cells at 0.5 mV s^{-1} . **b** LMN CE under full plating/stripping conditions at 0.5 mA cm^{-2} and 1 mAh cm^{-2} . **c** Modified Aurbach's

measurement of LMN CE. **d** Cycling performance of lean-Li Li||Li symmetric cells at 1 mA cm^{-2} and 3 mA cm^{-2} (DOD = 75%). All electrochemical tests are conducted at 30°C . **e** Comparisons of LMN CE with previously reported advanced electrolytes.

stark contrast, in the CI 7 electrolyte, the peak corresponding to large clusters at 0.9 \AA^{-1} completely disappears, which may be due to the presence of CIDE that disrupts these large solvation clusters, retaining only relatively smaller ones. Additionally, distinct small protrusions can be observed at around 2 and 2.5 \AA^{-1} (Corresponding to r values of 3.9 and 3.1 \AA), indicating the presence of shorter interatomic distances in the CI 7 electrolyte, which furthermore demonstrates the more tightly packed solvation clusters. Molecular dynamics simulations, NMR spectra, and WAXS all collectively demonstrate that the primary solvation shell in the CI7 electrolyte has been compressed by CIDE, resulting in the emergence of super anion-enriched and tightly knit solvation clusters. It is conceivable that our CI 7 electrolyte with anion-aggregated and compact solvation structure can deliver superior stability for LMN and cultivate a robust SEI enriched with inorganics, guaranteeing the longevity and reliability of LMB.

Reduction stability of electrolyte and reversibility of LMN

The compatibility of the electrolytes with LMN was initially assessed through cyclic voltammetry (CV) in the Li||Cu half cells. As presented

in Fig. 3a, in the low-concentration electrolyte (2 M LiFSI in DME, donated as 2 M electrolyte), a noticeable reduction decomposition current was observed, demonstrating the poor compatibility with LMN. By pushing the salt concentration close to the limit of saturation, the reduction decomposition of the electrolyte was significantly alleviated in the 10 M electrolyte. In sharp contrast, the reduction behavior of the CI 7 electrolyte, characterized by a tightly compressed solvation structure, is extremely suppressed, suggesting that this compressed solvation structure is inherently more stable with LMN. The smaller response current in the subsequent scan also confirms the weaker reactivity of the CI 7 electrolyte and the excellent protective function of the formed SEI. The reduction stability of the electrolytes was further verified by monitoring the corrosion current during a constant voltage process in Li||Cu cells (Supplementary Fig. 6). The rapid decline in corrosion current and minimal leakage current further demonstrate the quick passivation ability of the compressed Li-FSI⁻ clusters and the strongest protective capability of the derived SEI. The galvanostatic tests of the Li||Cu cells between 0–1 V also demonstrate the optimal compatibility between

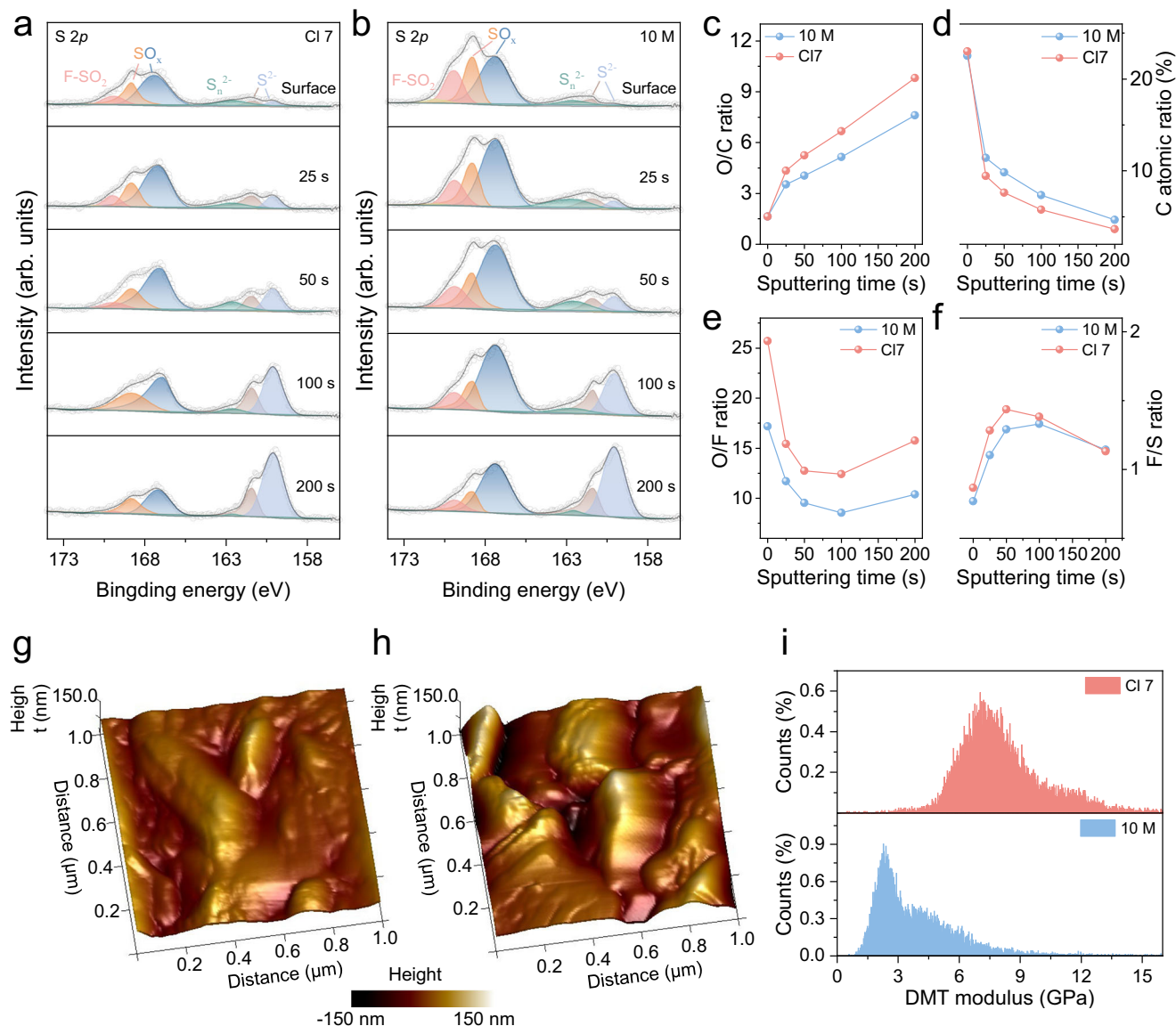


Fig. 4 | Analysis of the physicochemical and mechanical properties of the SEI. Etching XPS depth profiles of S 2p on deposited LMN in (a) Cl 7 and (b) 10 M electrolyte. The (c) O/C ratio, (e) O/F ratio and (f) F/S ratio and (d) C atomic ratio in 10 M and Cl 7 electrolyte at different depths. AFM morphology of SEI on deposited

Li in (g) Cl 7 and (h) 10 M electrolyte. i DMT modulus distribution of SEI in two electrolytes. The LMN used for XPS and AFM tests was obtained by deposited 3 mAh cm^{-2} Li at 0.5 mA cm^{-2} on Cu after cycling at 0.5 mA cm^{-2} and 2 mAh cm^{-2} for 10 cycles.

Cl 7 electrolyte and the LMN (Supplementary Fig. 7, Supplementary Note 2).

The reversibility of Li plating/stripping was further evaluated by coulombic efficiency (CE) measurement in Li||Cu cells. Under full plating/stripping conditions at a current density of 0.5 mA cm^{-2} and a fixed capacity of 1 mAh cm^{-2} , the 2 M, 10 M and Cl 7 electrolytes show initial CEs of 92.73%, 94.39%, and 97.81%, respectively (Supplementary Fig. 8), confirming the most inert reactivity of Cl 7 electrolyte towards Li metal negative electrode. Moreover, in the following repeated plating/stripping cycles, the CE measured in the Cl 7 electrolyte rapidly increased to 99% within 6 cycles, while those in 2 M and 10 M electrolytes need more than 20 cycles to climb to 99% (Supplementary Fig. 9). Notably, the Cl 7 electrolyte delivers an average CE of 99.48% over 500 cycles (Fig. 3b), higher than that for 10 M electrolyte (99.28%). In comparison, the 2 M electrolyte exhibited significant instability and substantial fluctuations within the 300 cycles. To evaluate the reactivity and stability of Li deposited in different electrolytes, we incorporated a 12-hour aging period

following Li deposition to allow the electrolytes to “corrode” the Li (Supplementary Fig. 10). Furthermore, taking into account the differences in Li deposition and SEI formation on Cu and Li substrates, the modified Aurbach’s method was also adopted to evaluate the plating/stripping efficiency on Li substrates, which is more appropriate for the practical application environments of LMB⁴³. As shown in Fig. 3c, the CE in the high-concentration 10 M electrolyte can achieve a relatively high value of 99.34%. However, in the Cl 7 electrolyte, the CE achieves 99.91%, and even after an additional 150 cycles at 0.5 mA cm^{-2} and 1 mAh cm^{-2} , the CE based on the fully passivated substrate can reach as high as 99.96%. Even adopting the general Aurbach protocol (5 mAh cm^{-2} for formation), our Cl 7 electrolyte still demonstrated a high CE of 99.84% (Supplementary Fig. 11). Moreover, even in carbonate ester-based electrolyte, which is inherently unstable towards Li metal, such as DMC-based electrolyte, good plating/stripping reversibility can still be achieved through compressed solvation structure (Supplementary Fig. 12, Supplementary Note 3). As far as we know, the high average CE more

than 99.9% is among state-of-the-art liquid-state electrolytes (Fig. 3e)^{3,12–14,17,19,27,28,31,32,44–53}.

In addition, the practical long-term stability to Li metal was further evaluated by Li||Li symmetric cells with 20 μm -thick Li sheets as electrodes. At 1 mA cm^{-2} and 3 mAh cm^{-2} , corresponding to a 75% depth of discharge (DOD), Li||Li cells with the Cl 7 electrolyte demonstrates an impressive cycle life exceeding 2000 h, which is in dramatic contrast to the brief cycles in cells employing 2 M and 10 M electrolytes due to swift Li depletion (Fig. 3d). At the condition of 50% DOD, the cell with Cl 7 electrolyte can even remain stable over 3200 h (Supplementary Fig. 13). The remarkable stability of lean-Li symmetric cells convincingly substantiates the stability of the compressed solvation clusters on LMN and the reliability of the associated SEI. Electrochemical impedance spectroscopy (EIS) was conducted subsequent to various aging intervals to further validate the stability of SEI (Supplementary Fig. 14). It is shown that the Li||Li cell within the Cl 7 electrolyte delivers the smallest R_{SEI} ascribed to the formation of SEI derived from compressed solvation clusters. As the aging time extends, the R_{SEI} in both 2 M and 10 M electrolytes shows a pronounced continuous increase due to the flimsy interphase, whereas the Cl 7 electrolyte exhibits only a slight increase in R_{SEI} value. This further validates the excellent compatibility of the Cl 7 electrolyte with LMN.

Li metal interface analysis and stacking morphology

The reactivity of Li metal with the electrolyte and the stacking morphology are closely associated with the SEI, we have delved deeply into the composition and structural information of the SEI. The disparities in SEI composition formed in various electrolytes were initially detected by in-depth X-ray photoelectron spectroscopy (XPS) (Fig. 4a–f and Supplementary Fig. 15–21). In fact, the types of SEI components formed in the Cl 7 electrolyte are analogous to those in the 10 M electrolyte, as both possess an anion-rich solvation structure that facilitates the generation of FSI-derived SEI. However, there are noticeable differences in the proportion of species and the trend of elemental changes. From the S 2p spectra (Fig. 4a) containing solely the decomposition products of the FSI^- anion, it can be seen that the outermost SEI of both has the same types of substances. Nevertheless, throughout the entire sputtering process, the SEI in the 10 M electrolyte consistently contains a higher amount of incompletely decomposed products of FSI^- , such as F-SO_x and S_n^{2-} . In contrast, in the Cl 7 electrolyte, the content of incomplete decomposition products in the SEI rapidly depletes, and Li_2S , the ultimate reduction product of FSI^- , becomes significantly dominant, evidencing the accelerated reduction kinetics of the FSI^- anion in the compressed solvation structure. Additionally, the consistently approaching F/S ratio of 1 in the SEIs demonstrates that the dissolution of anion-reduction products is minimized in both electrolytes, with variations in components principally depending on the reduction behavior of FSI^- anion. The higher O/C ratio, O/F ratio, along with results from the O 1s and Li 1s spectra, indicate that a more Li_2O -rich SEI forms in our Cl 7 electrolyte, which corroborates recent insights that a Li_2O -rich SEI is key for achieving high coulombic efficiency^{28,54}. Meanwhile, the weaker C-related signal ratio suggests that the proportion of organics generated from solvent reduction is markedly restricted in the Cl 7 electrolyte. Moreover, the consistently low levels of Cl throughout the etching process in the Cl 7 electrolyte indicate that ClDEE itself has excellent reduction stability, undergoing minimal reductive decomposition on the LMN, consistent with the reduction stability qualified by density functional theory (DFT) calculations (Supplementary Fig. 22 and Supplementary Data 2). The overall lower N and S intensity in the SEI further demonstrates that the compressed solvation structure and its derived SEI effectively suppress the continuous decomposition of the FSI^- anion, which is crucial for preserving a stable solvation structure and minimizing electrolyte consumption during long-term cycling. Cryogenic transmission electron microscopy (cryo-TEM) was

further employed to decipher the constituents and their spatial distributions in the SEIs (Supplementary Fig. 23–25). In the 2 M electrolyte, the SEI exhibits a notably larger thickness and unevenness, with sporadic distributions of tiny inorganic substances, indicating that the SEI is primarily composed of organic byproducts from solvent reduction. Conversely, in the anion-rich 10 M electrolyte, there is a significant increase in the amount of LiF and Li_2O produced by anion decomposition, yet it still exhibits a clearly irregular spatial distribution and a relatively thick profile. In the Cl 7 electrolyte, the formed SEI is thin and conformal, embedded with a great deal of uniformly distributed LiF and Li_2O nanocrystals. It can be deduced that this SEI, abundant in uniformly distributed LiF and Li_2O nanocrystals, can effectively facilitate homogeneous Li circulation and suppress side reactions between the electrolyte and Li metal.

Atomic force microscopy (AFM) was employed to probe the homogeneity and mechanical properties of SEIs. As shown in Fig. 4g and h, the SEI in the Cl 7 electrolyte demonstrates a significantly smoother surface topography. The amplitude of the SEI's surface undulations in the Cl 7 electrolyte is almost confined to less than 50 nm, whereas it exceeds 100 nm in the 10 M electrolyte (Supplementary Fig. 26). The average surface roughness is recorded at 17.1 nm in the Cl 7 electrolyte but it is 31.9 nm in the 10 M electrolyte, suggesting superior homogeneity of the SEI in the Cl 7 electrolyte. Additionally, the mechanical strength of the SEI, quantified by Derjaguin–Müller–Toporov (DMT) modulus, is substantially higher in the Cl 7 electrolyte, reaching 8.2 GPa, which is 2.1 times higher than that in the 10 M electrolyte (3.9 GPa) (Fig. 4i and Supplementary Fig. 27). The interphases characterization results collectively manifest that the compressed solvation structure in the Cl 7 electrolyte appears to enhance the deep reduction of anions, enabling rapid passivation of Li metal, and the resulting SEI, rich in LiF and Li_2O , exhibits a uniform morphology and robust mechanical strength.

We further scrutinized the deposition patterns of Li using scanning electron microscopy (SEM). The nucleation behavior of Li was first analyzed by depositing 0.1 mAh cm^{-2} of Li onto Cu substrates (Supplementary Fig. 28). In the 2 M electrolyte, the initial Li nuclei are noticeably tiny and whisker-like. As the Li salt concentration increased, nucleation in the 10 M electrolyte resulted in larger disc-shaped structures. In the Cl 7 electrolyte, the initial Li nuclei are the biggest and have the smoothest morphology. Statistical analysis of the size distribution of Li nuclei reveals that in the 2 M, 10 M, and Cl 7 electrolytes, the average diameters are 0.22, 0.46, and 0.85 μm , respectively, demonstrating the flattest Li deposition in the Cl 7 electrolyte. Then, the evolution of the morphology and thickness of Li during the Li plating and stripping process was analyzed in detail (Supplementary Figs. 29–32, Supplementary Note 4). It can be observed that as the salt concentration increased from 2 M to 10 M, the Li deposition morphology transitions from dendritic to large columnar structures. While Li in the 10 M electrolyte exhibits a plump root support, noticeable unevenness and grooves are still present at the top of the Li deposits. This irregularity becomes more pronounced during the stripping process. Partially stripped Li in the 2 M electrolyte shows significant spatial distribution disparities and localized filamentation. Local cracks and a rough surface are also observed in the 10 M electrolyte. Upon complete stripping, the surface of Cu in the 2 M electrolyte shows distinct Li residues and chaotic decomposition products, whereas in the 10 M electrolyte, the remnants are markedly reduced, but local protrusions are still evident. In stark contrast, Li deposited in the Cl 7 electrolyte maintains a compact and smooth morphology from top to bottom with minimal voids, and retains overall blockiness and connectivity during the stripping process. Especially after full Li stripping, the Cu in the Cl 7 electrolyte is covered by a uniformly dense SEI, with virtually no Li residue. The consistent maintenance of a dense Li stacking configuration in the Cl 7 electrolyte throughout the electroplating and stripping process should play a vital role in minimizing

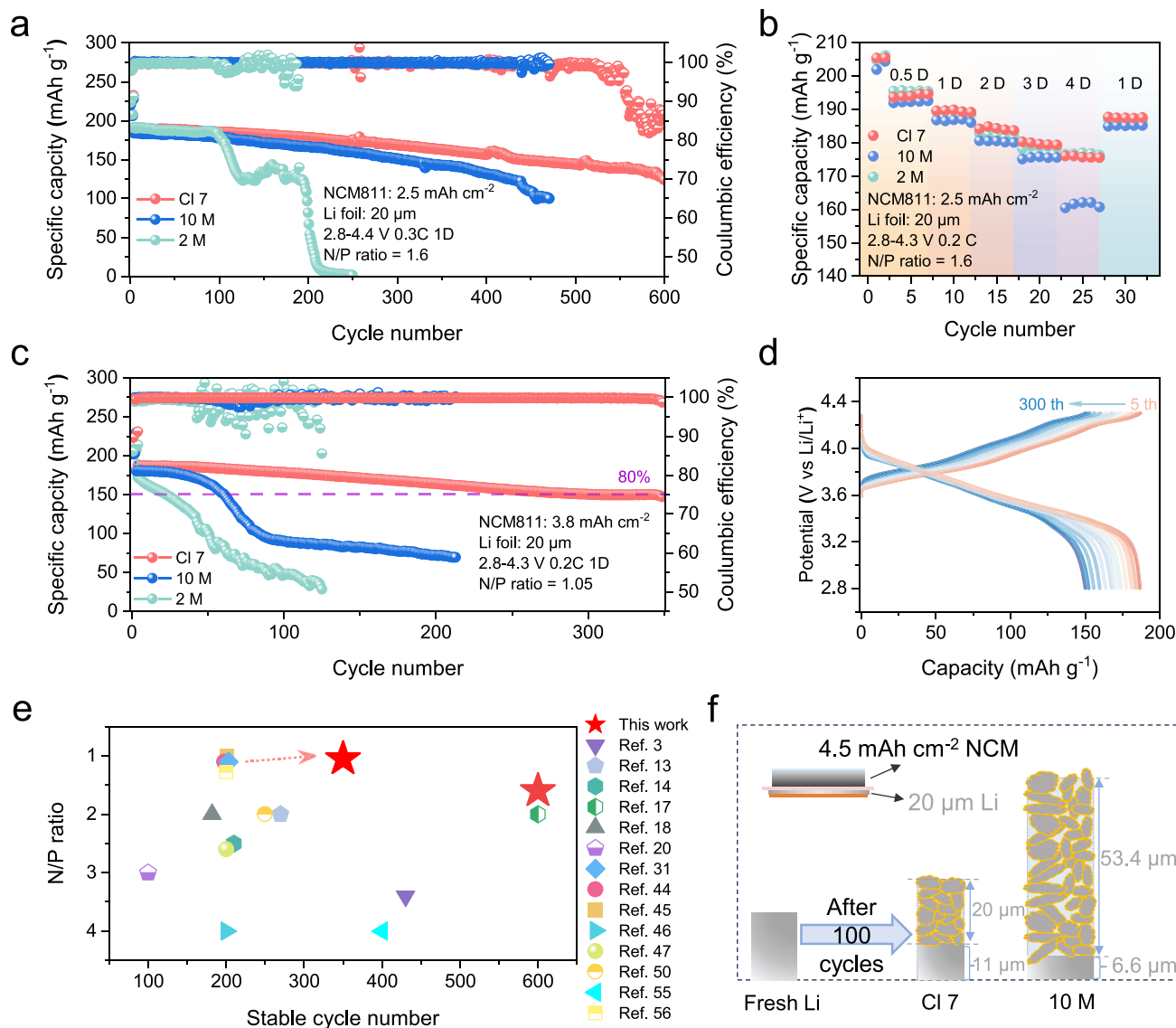


Fig. 5 | Li||NCM811 full cells performance and LMN evolution. Li||NCM811 full cell cycling performance with positive electrodes loading of (a) 2.5 and (c) 3.8 mAh cm⁻². **b** Rate performance of Li||NCM811 full cells with the electrolytes at 0.2 C charge/0.5–4 C discharge. 1 C = 200 mA g⁻¹. All electrochemical tests are conducted at 30 °C. **d** Evolution of voltage profiles in Li||NCM811 full cell (N/P

ratio=1.05) with CI 7 electrolyte. **e** Comparisons of electrochemical performance in LMB with lean-Li and high-loading-positive electrode in published literature and this work^{66,67}. **f** Schematic illustration of LMN expansion under harsh full cell conditions within different electrolytes.

Li depletion. SEM images captured at higher deposition levels and wider field views further confirm the more compact and seamless Li deposition pattern within the CI 7 electrolyte (Supplementary Fig. 33), which can minimize the active surface area available for side reactions on the Li metal surface.

Electrochemical performance of Li metal full cells

The tolerance of different electrolytes was initially examined by linear sweep voltammetry (LSV) in the Li||Al half cells (Supplementary Fig. 34). As expected, in the low-concentration 2 M electrolyte, the current began to increase sharply beyond 4.5 V due to aluminum corrosion and oxidative decomposition of the electrolyte. In high-concentration electrolyte, the tolerance to high voltage is significantly enhanced. This antioxidant property is also retained in CI 7 electrolyte, substantiated by the compatibility with NCM811 (Supplementary Fig. 35, Supplementary Note 5). In pursuit of high-energy-density Li metal batteries, the reliability of the electrolyte with compressed

solvation structure is evaluated under harsh full-battery conditions, including, ultrathin LMN (20 μm) and high-loading positive electrodes (2.5 mAh cm⁻² and 3.8 mAh cm⁻²). At an N/P ratio of 1.6 (Fig. 5a), “roll-over failure” occurs after merely 100 cycles in the 2 M electrolyte, while the “strengthened” 10 M electrolyte maintains 80% and 54% capacity retention after 300 and 471 cycles, respectively. In stark contrast, the cell with the CI 7 electrolyte obtains a substantial cycle life over 600 cycles, maintaining 80% and 70% capacity retention after 429 and 591 cycles, respectively. The full cell with CI 7 electrolyte simultaneously exhibits favorable high-rate discharge capability (Fig. 5b), indicating satisfactory interfacial dynamics. When the positive electrode loading is further increased to 3.8 mAh cm⁻² and the N/P ratio reaches 1.05 (Fig. 5c), the cell with the 2 M electrolyte suffers rapid degradation due to poor stability at both the negative electrode and positive electrode sides. In the 10 M electrolyte, a dramatic rise in polarization occurs after ~50 cycles, correlating with the sharp decrease in capacity (Supplementary Fig. 36). The full cell with the CI 7 electrolyte achieves ~80%

capacity retention after 350 cycles with slowly evolving overpotentials (Fig. 5d). Among the reported lean-Li, high-loading Li metal batteries, particularly with an N/P ratio close to 1, our Cl 7 electrolyte stands out with nearly the best performance (Fig. 5e). The superior stability to both negative electrode and positive electrode is further demonstrated in initially anode-free cell configuration (Supplementary Fig. 37). The Cl 7 electrolyte enables the Cu||NCM811 coin cell to achieve a CE exceeding 99.5%, with capacity retention rate of 70% and 60% after 90 and 140 cycles, markedly outperforming the 2 M and 10 M electrolytes.

SEM was conducted on the Li negative electrodes after cycling under harsher conditions in full cells (positive electrode loading is 4.5 mAh cm^{-2} , N/P ratio is 0.89) to grasp the morphology evolution of the Li negative electrodes (Fig. 5f). From the top-view SEM images (Supplementary Fig. 38), Li negative electrode cycled in Cl 7 electrolyte can still maintain a relatively flat and compact morphology at a large spatial scale, whereas Li negative electrode in the 10 M electrolyte exhibits substantial ravines and sparse accumulation, exposing more Li metal to side reactions with the electrolyte and thereby consuming active Li. The increased consumption of active Li and volume expansion are further demonstrated in the cross sectional-view SEM images (Supplementary Fig. 39). The Li negative electrode in the 10 M electrolyte has ballooned to a thickness of 60 μm , with only 6.6 μm of the original dense Li source remaining. In contrast, the Cl 7 electrolyte preserves over 11 μm of the initial compact Li layer, with the overall thickness swelling to a mere 31 μm . In addition, EIS was conducted after cycles in the full cells (N/P = 0.89) to confirm the evolution of interfacial dynamics (Supplementary Fig. 40). By decoupling the impedance into the resistance of electrode/electrolyte interphase (R_{SEI}) and the charge transfer resistance (R_{ct}), we found that the R_{SEI} for the cell using the 10 M electrolyte increased by 56.5% from the 50th cycle to 100th cycle, while the R_{SEI} with the Cl 7 electrolyte remained relatively stable and consistently lower. This indicates that the inorganic-rich, robust interfacial film derived from the compressed solvation structure possesses superior stability and excellent protective effects, suppressing the continuous breakdown of the electrolyte and the thickening of the interfacial film. The R_{ct} , however, demonstrated a downward trend in the 10 M electrolyte. In conjunction with the morphological evolution of the Li negative electrode, we correlate with the jagged deposition pattern of Li metal that enlarges the active surface area, consequently lowering R_{ct} . The above results demonstrate that the Cl 7 electrolyte with compressed solvation structure not only exhibits exceptionally superior stability on the Li metal negative electrode side but also shows excellent tolerance for NCM811.

High-energy-density Li metal pouch cell performance

Motivated by the remarkable reversibility of Li plating/stripping and the favorable compatibility with NCM811 in our compressed solvation structure electrolyte, we proceeded to evaluate its practical feasibility in a Li metal pouch cell. In pursuit of maximum available specific energy, raising the proportion of active positive electrode material across all components is the key. To fulfill this intention, we have meticulously optimized the parameter design, adopting 100 μm Li foil as the negative electrode devoid of Cu collectors, 30 mg cm^{-2} high-loading NCM811 positive electrodes, lean electrolyte of 1.1 g Ah^{-1} and minimalization of other non-active mass (Fig. 5a, b). Following this, the 5.6 Ah Li metal pouch cell with Cl 7 electrolyte delivers a high specific energy of 510.3 Wh kg^{-1} based on the total weight of all parts at 0.1 C, and retains a capacity/energy retention of 84%/83% after 116 cycles at 0.1 C charge/0.25 C discharge (Fig. 5c). The aggressive design parameters of our Li metal pouch cell almost reach the threshold of positive electrode material proportion (68%) and the specific energy ceiling at this capacity, outperforming the majority of state-of-the-art high-energy-density Li metal pouch cells reported. This outcome firmly confirms the extraordinary stability of our compressed solvation

structure electrolyte for LMN, which can withstand extremely high-capacity Li plating/stripping and curb electrolyte depletion, showcasing significant practical application potential in the LMB technology.

In summary, by compressing the primary solvation shell of Li ions through the minimally coordinated second phase CIDE, Li ions form tighter solvation clusters with FSI⁻ anions, resulting in an unprecedented high concentration of Li salts in the solvent phase. This compressed solvation structure confers exceptional stability on LMN and facilitates the rapid decomposition of Li salts to form a robust and homogenous SEI rich in LiF and Li₂O, advancing Li metal plating/stripping efficiency up to 99.9%. Empowered by this compressed solvation structure, not only do the lean-Li Li metal coin cells demonstrate superior long cycling life, but also the Li metal pouch cell of 510.3 Wh kg^{-1} with a high positive electrode proportion has steadily operated over 100 cycles. Our proposed strategy of compressed solvation structure propels the advancement of anion-rich electrolytes, presenting a promising approach for highly reversible LMN.

Methods

Materials

LiFSI (99.9%), DME (99.9%), DMC (99.9%), polyvinylidene difluoride (PVDF 5130, Mw=1300000), and N-methylpyrrolidone (NMP, >99.0%) were purchased from Suzhou Duoduo Chemical Technology Co. CIDE (>99.0%) was purchased from TCI Chemical Co. All solvents were stored over 4 Å molecular sieves for 72 h before use. All of the electrolytes were prepared in a glove box filled with argon gas ($\text{O}_2 < 0.01 \text{ ppm}$, $\text{H}_2\text{O} < 0.01 \text{ ppm}$). Li foils (20 μm , 100 μm , and 450 μm in thickness, Li content $\geq 99.9\%$) were purchased from China Energy Lithium Co. Polyethylene (PE) separator was purchased from Asahi Kasei Technosystem Co. Carbon black (Super P), aluminum foil, 2032-type coin-cell cases, springs, and spacers were purchased from Kelude Co, Ltd. Single-crystal NCM811 particles were obtained from Ronbay Technology. NCM811 positive electrodes (2.5 mAh cm^{-2} and 3.8 mAh cm^{-2}) were prepared by casting the slurry consisting of 96 wt% NCM811, 2 wt% Super P, and 2 wt% PVDF in NMP onto aluminum foil. In the pouch cell, the positive electrode consists of NCM811, conductive carbon, and PVDF binder in a weight ratio of 96.8:1.7:1.5. The electrode sheets were coated using a doctor blade coater (MSK-AFA-III, Hefei-Kejing Materials Technology Co., Ltd). The electrode sheets were then cut to the corresponding size using a battery splitter (T07, Hefei-Kejing Materials Technology Co., Ltd).

Cell assembly and electrochemical tests

2032 type coin cells were assembled in a glove box filled with argon gas ($\text{O}_2 < 0.01 \text{ ppm}$, $\text{H}_2\text{O} < 0.01 \text{ ppm}$). All electrolyte preparations were carried out in the same glovebox. The molar ratio of LiFSI, DME, and CIDE in the Cl 7 electrolyte is 1.6:1:6. The molar ratio of LiFSI to DME in the 2 M electrolyte is 1:5. The molar ratio of LiFSI to DME in the 10 M electrolyte is 1:1. Li||Cu coin cells consist of Li foil (thickness: 450 μm , diameter: 15.6 mm), PE separators (thickness: 20 μm , diameter: 19 mm), and Cu foil (thickness: 10 μm , diameter: 19 mm). Li||NCM811 coin cells consist of thin Li foil (thickness: 20 μm , diameter: 14 mm, on 6 μm Cu foil), PE separators, and NCM811 positive electrodes (loading: 2.5, 3.8, or 4.5 mAh cm^{-2} , diameter: 12 mm). Li||Li coin cells consist of thin Li foil (thickness: 20 μm , diameter: 14 mm, on 6 μm Cu foil) and PE separators. 50 μL electrolyte was adding in all coin cells. The coin cells were sealed by a manual battery hydraulic sealer sealing machine with a pressure of 800 psi.

Galvanostatic charge/discharge tests were carried out using a Neware battery cycler (CT-4008) at 30 °C in a climatic chamber. For Li||Cu coin cells, the modified Aurbach method was as follows: (1) plating 1 mAh cm^{-2} Li on Cu and charging until 1 V at 0.5 mA cm^{-2} five times to passivate the Cu collector (2) plating 5 mAh cm^{-2} Li at 0.5 mA cm^{-2} on Cu; (3) charging to 1 mAh cm^{-2} at 0.5 mA cm^{-2} and then discharging to 1 mAh cm^{-2} at 0.5 mA cm^{-2} for 10 cycles; (4) charging to 1 V at

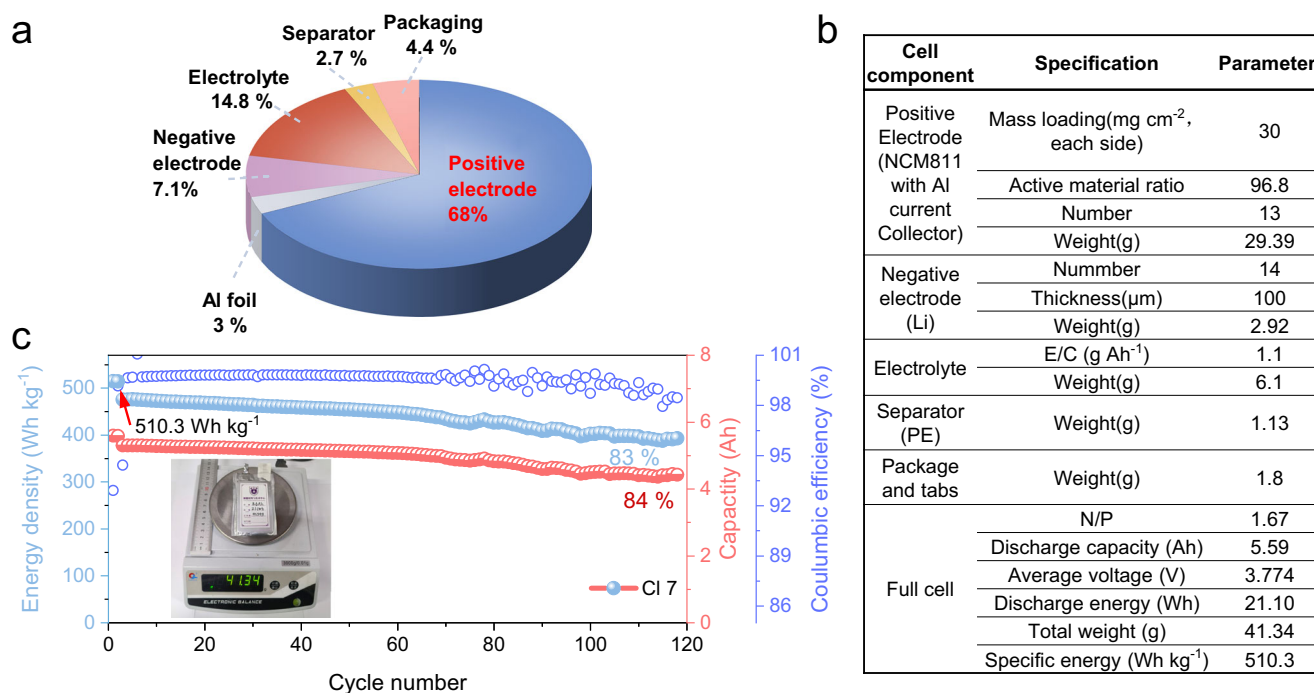


Fig. 6 | Electrochemical performance of 510.3 Wh kg⁻¹ Li metal pouch cell with ultra-high positive electrode ratio. a Mass distribution of all cell components in the pouch cell. **b** Detail parameters of the Li metal pouch cell. **c** Cycling

performance of the Li metal pouch cell at 0.1 C charge/0.25 C discharge after the initial two cycles at 0.1 C charge/discharge. 1 C = 0.55 A. All electrochemical tests are conducted at 30 °C.

0.5 mA cm⁻² to stripping all remaining Li on Cu. The cycle CE was measured by plating/stripping 1 mAh cm⁻² Li repeatedly at 0.5 mA cm⁻² with a charge cut-off voltage of 1 V. For Li||NCM811 coin cells, two initial cycles at 0.1 C for activation were conducted, and then cycled at different currents for long-term tests.

The Li||NCM811 pouch cell was assembled in a dry room with a dew point below -60 °C at a temperature of 10 °C. To minimize the mass of inactive materials, we adopted 10 μm aluminum foil as the positive electrode current collector, with high-loading positive electrodes of 30 mg cm⁻² on each side, 12 μm PE separator (86 cm lateral width, 45 ± 5% porosity), 100 μm Li metal foil as the negative electrode without Cu current collector, and an 86 μm aluminum plastic film for the external packaging. The positive electrode has a compaction density of 3.4 g cm⁻³ and a porosity of approximately 30%. The detailed parameter is presented in Fig. 6b. The electrolyte was injected through a pipettor. The pouch cell was vacuum sealed at 170 °C under -90 kPa. To ensure optimal electrolyte infiltration, the pouch cell is left to stand at 30 °C for over 36 hours after electrolyte filling, without applying external pressure, to facilitate uniform electrolyte distribution. The pouch cell was tested at 0.1 C for charging and 0.25 C for discharging after two formation cycles at 0.1 C with an initial pressure of about 200 kPa at 30 °C.

For LSV and CV test, Li||Al cells and Li||Cu cells were tested by an electrochemical workstation (CHI760E, Chenhua Co., Ltd) with different voltage ranges respectively. The EIS tests for Li||Li cells and Li||NCM811 cells were conducted on Solartron1260/1287 with a frequency range from 1 MHz to 0.01 Hz and an amplitude of 5 mV (potentiostatic, Steps/Decade=10, quasi-stationary potential).

Material characterizations

⁷Li nuclear magnetic resonance (NMR) spectra were obtained on a BRUKER 600 Nuclear Magnetic Resonance spectrometer. WAXS measurements were performed on Xeuss3.0 (Xenocs, France) with a Cu X-ray source of 30 W (wave length of 0.1542 nm) and a detector of Pilatus 300 K (Dectris). The sample-detector distance was set to

538 mm to cover a broad Q range by using the virtual detector mode. The 1-D scattering profiles were reduced from the 2-D data using the XSACT package.

To observe the morphology of Li deposition and obtain information related to the SEI, the cycled Li||Cu and Li||NCM811 coin cells were disassembled in the Ar-filled glovebox and the electrodes were washed in DME to remove the residual electrolyte. Li deposition morphology in Li||Cu cells and Li morphology evolution in Li||NCM811 cells was characterized by SEM at 2.0 kV (FESEM, Hitachi SU8010). X-ray photoelectron spectroscopy (XPS) measurement was collected on a PHI 5000 VersaProbe (Ulvac-Phi Co.). Ar ions were used to sputter for in-depth XPS tests and all samples were prepared and sealed into XPS transfer chamber in Ar filled glovebox before XPS measurement without being exposed to ambient air. The roughness and mechanical properties of SEI were tested on Dimension Icon Atomic Force Microscope. For cryo-TEM characterization, Li was deposited onto a lacey carbon grid in Li||Cu coin cells at 0.5 mA cm⁻² for 20 min. The grids with Li were lightly rinsed with DME, then were placed into TEM sample cassette and sealed under argon gas. Subsequently, they were transferred to a TEM column immersing in liquid nitrogen without exposed to air. FEI Glacios (USA) operated at 200 kV equipped with automatic injection system of frozen sample was performed to collect images. The procedures for the preparation of the electrode or electrolyte samples were conducted in a glove box filled with argon gas (O₂ < 0.01 ppm, H₂O < 0.01 ppm) at 23 ± 5 °C, and the samples were sealed in an argon atmosphere without exposure to air during the transfer process.

Theoretical calculations

The classical molecular dynamics (MD) simulations were carried out using GROMACS⁵⁵ to understand the electrolytes designed in this work. The AMBER-99 force field^{56,57} was used along with the Restrained Electro Static Potential (RESP) charge generated by Multiwfn^{58,59}. The linear constraint solver (LINCS) algorithm^{60,61} was used to constrain the bonds with hydrogen atoms. Initially, 150 DME, 150 LiFSI molecules

were packed into a $38 \times 38 \times 38 \text{ \AA}^3$ cubic box using the packmol⁶² software to simulate the system of 10 M electrolyte. For the Cl 7 electrolyte, 42 DME, 70 LiFSI, and 263 CLDEE molecules were packed. Initially, all systems were heated from 10 K to their respective target temperatures—298.15 K for room temperature (RT) and 253.15 K for low temperature (low T)—over a period of 100 ps. This was followed by a 5-ns equilibration phase under isothermal-isobaric (NPT) conditions at 1 bar. For the production phase, an additional 10 ns of NPT simulations were conducted. All MD simulations were performed with a time step of 1 fs. During NPT simulations, the temperature was regulated using a Nosé-Hoover thermostat⁶³ with a time constant of 2 ps, while the pressure was maintained via C-rescale coupling with a coupling constant of 5 ps. Electrostatic interactions were managed using the Particle-Mesh-Ewald (PME) method, employing a cut-off distance of 1.3 nm^{64,65}.

Reduction potentials were computed using the PCM(ether)/ ω B97XD/6-31 + G(d,p) model chemistry using Gaussian 16 C.02. All the structures were first optimized until the maximum force converged into 0.00045 a.u., and later the molecular orbitals were retrieved from the output files of Gaussian 16 program. The reference state used for hydrogen is H_2 in the gas phase. The reduction/oxidation potentials were calculated following the equation as

$$E^{\text{re/ox}} = \pm \frac{\Delta G(A \rightarrow A^\pm)}{nF} - 1.4$$

The numerator is the free energy difference between the reduced or oxidized species and the neutral species, the denominator is the product of Faraday's constant and the number of electrons (always one in this case). The 1.4 accounts for shifting the computed potential towards Li^+/Li scale. This is derived using a value of 4.44 V for the standard hydrogen electrode and the -3.04 V standard reduction potential of Li.

Data availability

The datasets generated and analyzed in this work are included in this article and Supplementary Information. Source data are provided with this paper.

References

- Liu, J. et al. Pathways for practical high-energy long-cycling lithium metal batteries. *Nat. Energy* **4**, 180–186 (2019).
- Lin, D., Liu, Y. & Cui, Y. Reviving the lithium metal anode for high-energy batteries. *Nat. Nanotechnol.* **12**, 194–206 (2017).
- Zhang, Q.-K. et al. Homogeneous and mechanically stable solid–electrolyte interphase enabled by trioxane-modulated electrolytes for lithium metal batteries. *Nat. Energy* **8**, 725–735 (2023).
- Chen, S. et al. Critical parameters for evaluating coin cells and pouch cells of rechargeable Li-metal batteries. *Joule* **3**, 1094–1105 (2019).
- Niu, C. et al. Balancing interfacial reactions to achieve long cycle life in high-energy lithium metal batteries. *Nat. Energy* **6**, 723–732 (2021).
- Wan, H., Xu, J. & Wang, C. Designing electrolytes and interphases for high-energy lithium batteries. *Nat. Rev. Chem.* **8**, 30–44 (2024).
- Peled, E. The electrochemical behavior of alkali and alkaline earth metals in nonaqueous battery systems—the solid electrolyte interphase model. *J. Electrochem. Soc.* **126**, 2047 (1979).
- Hobold, G. M. et al. Moving beyond 99.9% Coulombic efficiency for lithium anodes in liquid electrolytes. *Nat. Energy* **6**, 951–960 (2021).
- Qian, J. et al. High rate and stable cycling of lithium metal anode. *Nat. Commun.* **6**, 6362 (2015).
- Fan, X. et al. Highly fluorinated interphases enable high-voltage Li-metal batteries. *Chem* **4**, 174–185 (2018).
- Ren, X. et al. Enabling high-voltage lithium-metal batteries under practical conditions. *Joule* **3**, 1662–1676 (2019).
- Cao, X. et al. Monolithic solid–electrolyte interphases formed in fluorinated orthoformate-based electrolytes minimize Li depletion and pulverization. *Nat. Energy* **4**, 796–805 (2019).
- Yu, Z. et al. Rational solvent molecule tuning for high-performance lithium metal battery electrolytes. *Nat. Energy* **7**, 94–106 (2022).
- Yu, Z. et al. Molecular design for electrolyte solvents enabling energy-dense and long-cycling lithium metal batteries. *Nat. Energy* **5**, 526–533 (2020).
- Xue, W. et al. Ultra-high-voltage Ni-rich layered cathodes in practical Li metal batteries enabled by a sulfonamide-based electrolyte. *Nat. Energy* **6**, 495–505 (2021).
- Yang, W. et al. Tailoring the electrode–electrolyte interface for reliable operation of all-climate 4.8 V Li||NCM811 batteries. *Angew. Chem. Int. Ed. n/a* (n/a), e202410893.
- Li, A.-M. et al. Methylation enables the use of fluorine-free ether electrolytes in high-voltage lithium metal batteries. *Nat. Chem.* **16**, 922–929 (2024).
- Chen, Y. et al. Steric effect tuned ion solvation enabling stable cycling of high-voltage lithium metal battery. *J. Am. Chem. Soc.* **143**, 18703–18713 (2021).
- Huang, Y. et al. Eco-friendly electrolytes via a robust bond design for high-energy Li metal batteries. *Energy Environ. Sci.* **15**, 4349–4361 (2022).
- Xia, Y. et al. Designing an asymmetric ether-like lithium salt to enable fast-cycling high-energy lithium metal batteries. *Nat. Energy* **8**, 934–945 (2023).
- Zhang, Q.-K. et al. Reforming the uniformity of solid electrolyte interphase by nanoscale structure regulation for stable lithium metal batteries. *Angew. Chem. Int. Ed.* **62**, e202306889 (2023).
- Yang, Y. et al. Liquefied gas electrolytes for wide-temperature lithium metal batteries. *Energy Environ. Sci.* **13**, 2209–2219 (2020).
- Yin, Y. et al. Fire-extinguishing, recyclable liquefied gas electrolytes for temperature-resilient lithium-metal batteries. *Nat. Energy* **7**, 548–559 (2022).
- Yang, Y. et al. High-efficiency lithium-metal anode enabled by liquefied gas electrolytes. *Joule* **3**, 1986–2000 (2019).
- Xu, Y. et al. Direct in situ measurements of electrical properties of solid–electrolyte interphase on lithium metal anodes. *Nat. Energy* **8**, 1345–1354 (2023).
- Zhao, Q., Stalin, S. & Archer, L. A. Stabilizing metal battery anodes through the design of solid electrolyte interphases. *Joule* **5**, 1119–1142 (2021).
- Wu, M. et al. High-performance lithium metal batteries enabled by a fluorinated cyclic ether with a low reduction potential. *Angew. Chem. Int. Ed.* **62**, e202216169 (2023).
- Zhao, Y. et al. Electrolyte engineering for highly inorganic solid electrolyte interphase in high-performance lithium metal batteries. *Chem* **9**, 682–697 (2023).
- Wu, Z. et al. Deciphering and modulating energetics of solvation structure enables aggressive high-voltage chemistry of Li metal batteries. *Chem* **9**, 650–664 (2023).
- Zhu, C. et al. Anion–diluent pairing for stable high-energy Li metal batteries. *ACS Energy Lett.* **7**, 1338–1347 (2022).
- Zhang, S. et al. Tackling realistic Li^+ flux for high-energy lithium metal batteries. *Nat. Commun.* **13**, 5431 (2022).
- Cao, X. et al. Effects of fluorinated solvents on electrolyte solvation structures and electrode/electrolyte interphases for lithium metal batteries. *Proc. Natl Acad. Sci.* **118**, e2020357118 (2021).
- Ding, J.-F. et al. Non-solvating and low-dielectricity cosolvent for anion-derived solid electrolyte interphases in lithium metal batteries. *Angew. Chem. Int. Ed.* **60**, 11442–11447 (2021).

34. Yoo, D.-J., Yang, S., Kim, K. J. & Choi, J. W. Fluorinated aromatic diluent for high-performance lithium metal batteries. *Angew. Chem. Int. Ed.* **59**, 14869–14876 (2020).
35. Jiang, Z. et al. Fluorobenzene, a low-density, economical, and bifunctional hydrocarbon cosolvent for practical lithium metal batteries. *Adv. Funct. Mater.* **31**, 2005991 (2021).
36. Cui, Z. et al. Molecular anchoring of free solvents for high-voltage and high-safety lithium metal batteries. *Nat. Commun.* **15**, 2033 (2024).
37. Qin, M. et al. Dipole–dipole interactions for inhibiting solvent co-intercalation into a graphite anode to extend the horizon of electrolyte design. *Energy Environ. Sci.* **16**, 546–556 (2023).
38. Weast, R. C., *CRC handbook of chemistry and physics*. 1st Student ed.; CRC Press: Boca Raton, FL, 1988.
39. Zou, Y. et al. Non-flammable electrolyte enables high-voltage and wide-temperature lithium-ion batteries with fast charging. *Angew. Chem. Int. Ed.* **62**, e202216189 (2023).
40. Liu, X. et al. Anchored weakly-solvated electrolytes for high-voltage and low-temperature lithium-ion batteries. *Angew. Chem. Int. Ed.* **63**, e202406596 (2024).
41. Kim, S. C. et al. High-entropy electrolytes for practical lithium metal batteries. *Nat. Energy* **8**, 814–826 (2023).
42. Liu, X., Fang, L., Lyu, X., Winans, R. E. & Li, T. Unveiling the liquid electrolyte solvation structure by small angle X-ray scattering. *Chem. Mater.* **35**, 9821–9832 (2023).
43. Adams, B. D., Zheng, J., Ren, X., Xu, W. & Zhang, J.-G. Accurate determination of coulombic efficiency for lithium metal anodes and lithium metal batteries. *Adv. Energy Mater.* **8**, 1702097 (2018).
44. Zhang, G. et al. A monofluoride ether-based electrolyte solution for fast-charging and low-temperature non-aqueous lithium metal batteries. *Nat. Commun.* **14**, 1081 (2023).
45. Zhao, Y., Zhou, T., Mensi, M., Choi, J. W. & Coskun, A. Electrolyte engineering via ether solvent fluorination for developing stable non-aqueous lithium metal batteries. *Nat. Commun.* **14**, 299 (2023).
46. Zhao, Y. et al. Fluorinated ether electrolyte with controlled solvation structure for high voltage lithium metal batteries. *Nat. Commun.* **13**, 2575 (2022).
47. Wu, L.-Q. et al. Unveiling the role of fluorination in hexacyclic coordinated ether electrolytes for high-voltage lithium metal batteries. *J. Am. Chem. Soc.* **146**, 5964–5976 (2024).
48. Sun, C. et al. Reduction-tolerance electrolyte design for high-energy lithium batteries. *Angew. Chem. Int. Ed.* **63**, e202400761 (2024).
49. Chen, J. et al. Hybridizing carbonate and ether at molecular scales for high-energy and high-safety lithium metal batteries. *Nat. Commun.* **15**, 3217 (2024).
50. Li, Z. et al. Non-polar ether-based electrolyte solutions for stable high-voltage non-aqueous lithium metal batteries. *Nat. Commun.* **14**, 868 (2023).
51. Kwon, H. et al. Borate–pyran lean electrolyte-based Li-metal batteries with minimal Li corrosion. *Nat. Energy* **9**, 57–69 (2024).
52. Kim, S. C. et al. Data-driven electrolyte design for lithium metal anodes. *Proc. Natl Acad. Sci.* **120**, e2214357120 (2023).
53. Tan, L. et al. Intrinsically nonflammable ether electrolytes for ultrahigh-voltage lithium metal batteries enabled by chlorine functionality. *Angew. Chem. Int. Ed.* **61**, e202203693 (2022).
54. Hobold, G. M., Wang, C., Steinberg, K., Li, Y. & Gallant, B. M. High lithium oxide prevalence in the lithium solid–electrolyte interphase for high Coulombic efficiency. *Nat. Energy* **9**, 580–591 (2024).
55. Abraham, M. J. et al. GROMACS: High performance molecular simulations through multi-level parallelism from laptops to super-computers. *SoftwareX* **1–2**, 19–25 (2015).
56. Chen, A. A. & Pappu, R. V. Parameters of monovalent ions in the AMBER-99 Forcefield: Assessment of inaccuracies and proposed improvements. *J. Phys. Chem. B* **111**, 11884–11887 (2007).
57. Wang, J., Cieplak, P. & Kollman, P. A. How well does a restrained electrostatic potential (RESP) model perform in calculating conformational energies of organic and biological molecules? *J. Comput. Chem.* **21**, 1049–1074 (2000).
58. Lu, T. & Chen, F. Multiwfn: A multifunctional wavefunction analyzer. *J. Comput. Chem.* **33**, 580–592 (2012).
59. Lu Tian, C. F.-W. Comparison of computational methods for atomic charges. *Acta Phys. -Chim. Sin.* **28**, 1–18 (2011).
60. Hess, B., Bekker, H., Berendsen, H. J. C. & Fraaije, J. G. E. M. LINCS: A linear constraint solver for molecular simulations. *J. Comput. Chem.* **18**, 1463–1472 (1997).
61. Hess, B. P-LINCS: A parallel linear constraint solver for molecular simulation. *J. Chem. Theory Comput.* **4**, 116–122 (2008).
62. Martínez, L., Andrade, R., Birgin, E. G. & Martínez, J. M. PACKMOL: a package for building initial configurations for molecular dynamics simulations. *J. Comput. Chem.* **30**, 2157–2164 (2009).
63. Posch, H. A., Hoover, W. G. & Vesely, F. J. Canonical dynamics of the Nosé oscillator: Stability, order, and chaos. *Phys. Rev. A* **33**, 4253 (1986).
64. Darden, T., York, D. & Pedersen, L. Particle mesh Ewald: An N-log(N) method for Ewald sums in large systems. *J. Chem. Phys.* **98**, 10089–10092 (1993).
65. Essmann, U. et al. A smooth particle mesh Ewald method. *J. Chem. Phys.* **103**, 8577–8593 (1995).
66. Huang, Z. et al. A salt-philic, solvent-phobic interfacial coating design for lithium metal electrodes. *Nat. Energy* **8**, 577–585 (2023).
67. Kim, S. et al. Wide-temperature-range operation of lithium-metal batteries using partially and weakly solvating liquid electrolytes. *Energy Environ. Sci.* **16**, 5108–5122 (2023).

Acknowledgements

This research was supported by the National Key R&D Program of China (2021YFB3800300—P.H. and H.Z.), the National Natural Science Foundation of China (No. 92372201—H.Z. and No.22239002—H.Z.), and the Science and Technology innovation fund for emission peak and carbon neutrality of Jiangsu province (BK20220034—H.Z. and BK20231512—P.H.).

Author contributions

H.Z. and P.H. conceived the idea and supervised the research. W.Y. conducted the experiments. A.C. conducted the SEM. W.Y. and H.Z. analyzed the experiment results and wrote the manuscript. P.H. discussed the results and commented on the manuscript.

Competing interests

The authors declare no competing interests.

Additional information

Supplementary information The online version contains supplementary material available at <https://doi.org/10.1038/s41467-025-59563-y>.

Correspondence and requests for materials should be addressed to Ping He or Haoshen Zhou.

Peer review information *Nature Communications* thanks Xi Chen, and the other, anonymous, reviewer(s) for their contribution to the peer review of this work. A peer review file is available.

Reprints and permissions information is available at <http://www.nature.com/reprints>

Publisher's note Springer Nature remains neutral with regard to jurisdictional claims in published maps and institutional affiliations.

Open Access This article is licensed under a Creative Commons Attribution-NonCommercial-NoDerivatives 4.0 International License, which permits any non-commercial use, sharing, distribution and reproduction in any medium or format, as long as you give appropriate credit to the original author(s) and the source, provide a link to the Creative Commons licence, and indicate if you modified the licensed material. You do not have permission under this licence to share adapted material derived from this article or parts of it. The images or other third party material in this article are included in the article's Creative Commons licence, unless indicated otherwise in a credit line to the material. If material is not included in the article's Creative Commons licence and your intended use is not permitted by statutory regulation or exceeds the permitted use, you will need to obtain permission directly from the copyright holder. To view a copy of this licence, visit <http://creativecommons.org/licenses/by-nc-nd/4.0/>.

© The Author(s) 2025